

Extended X-ray emission from radio galaxy cocoons

Biman B. Nath*

Raman Research Institute, Sadashiva Nagar, Bangalore 560080, India

Accepted 2010 May 19. Received 2010 May 19; in original form 2010 February 13

ABSTRACT

We study the emission of X-rays from lobes of FR-II radio galaxies by inverse Compton scattering of microwave background photons. Using a simple model that takes into account injection of relativistic electrons, their energy losses through adiabatic expansion, synchrotron and inverse Compton emission, and also the stopping of the jet after a certain time, we study the evolution of the total X-ray power, the surface brightness, angular size of the X-ray bright region and the X-ray photon index, as functions of time and cocoon size, and compare the predictions with observations. We find that the radio power drops rapidly after the stopping of the jet, with a shorter time-scale than the X-ray power. The X-ray spectrum initially hardens until the jet stops because the steepening of electron spectrum is mitigated by the injection of fresh particles, for electrons with $\gamma \geq 10^3$. This happens because of the concurrence of two times scales, that of the typical jet lifetimes and cooling due to inverse Compton scattering ($\sim 10^{7-8}$ yr), of electrons responsible for scattering CMB photons into keV range photons (with $\gamma \sim \sqrt{1 \text{ keV}/kT_{CMB}}$). Another finding is that the ratio of the X-ray to radio power is a robust parameter that varies mostly with redshift and ambient density, but is weakly dependent on other parameters. We also determine the time-averaged ratio of X-ray to radio luminosities (at 1 keV and 151 MHz) and find that it scales with redshift as $\propto (1+z)^{3.8}$, for typical values of parameters. We then estimate the X-ray luminosity function of FR-II radio galaxies and estimate the number of these diffuse X-ray bright objects above a flux limit of $\sim 3 \times 10^{-16}$ erg cm^{-2} s^{-1} to be ~ 25 deg^{-2} .

Key words: galaxies: active – galaxies: intergalactic medium – X-rays: galaxies

1 INTRODUCTION

A number of radio galaxies have been observed to emit diffuse X-rays in the region between the nucleus and radio hot spots in recent years. This emission has been interpreted as inverse-Compton scattering of the cosmic microwave background (CMB) photons by relativistic electrons in the radio lobes that have lost most of their energy and their Lorentz factor have come down to $\gamma \sim 10^3$ (Fabian et al. 2003; Blundell et al. 2006; Erlund et al. 2008; Johnson et al. 2007; Croston et al. 2005; Fabian et al. 2009; Isobe et al. 2009). That relativistic electrons in radio galaxy cocoons could upscatter CMB photons to X-rays has long been anticipated since the discovery of CMB (e.g., Felten & Rees 1967).

Since the increase in the CMB energy density with redshift ($\propto (1+z)^4$) compensates for the cosmological surface brightness dimming, this extended emission has been seen at both low and high redshift, and has been used as a probe

of the relativistic plasma in the lobe. Combined with radio observations, this emission provides constraints on the magnetic field and on the energy distribution among the relativistic particles, or both. While electrons with $\gamma \geq 10^4$ to emit GHz synchrotron radiation (for typical magnetic fields of a few μG), it requires $\gamma \sim 10^3$ to upscatter the CMB photons to the observed 1–10 keV range in X-rays.

The simultaneous radiation in two different wavelengths caused by the same parent electron population provides an excellent opportunity to probe the physical nature of the radiating object. Comparing the X-ray and radio emission from lobes, Blundell et al. (2006) showed that the injected electron energy distribution have a low-energy turn-over at $\gamma_{min} \geq 10^3$, since the X-ray bright regions did not coincide with the radio hot spots. The comparison between X-ray and radio studies also shed light on the magnetic field. Croston et al. (2005) argued that the inferred magnetic field strength is close to the equipartition value (lying between 0.3–1.3 times the equipartition value).

In this paper, we use a variant of a model of emission from FR-II radio galaxies advocated by Kaiser & Alexan-

* biman@rri.res.in

der (1997) (hereafter KA97) and Kaiser, Dennett-Thorpe & Alexander (1997) (hereafter KDA97) to study the evolution of X-ray power and surface brightness with time, and as functions of the radio lobe size, ambient density, redshift and the jet power. We do not assume self-similarity of the evolution of the radio lobe assumed by KA97 and KDA97, in order to study the effect of the cessation of jet activity on the X-ray surface brightness.

The evolution of radio lobes after the stopping of jets has been discussed by Komissarov & Gubanov (1994), although they did not address the soft X-ray emission by old electrons. Kaiser & Cotter (2002) have also discussed the evolution of radio galaxies in connection with the observations of radio relics, and Reynolds et al. (2002) have numerically studied the expansion of 'dead' radio galaxies.

We first discuss the KA97 and KDA97 model and the changes introduced in the model in the present paper, and then discuss the results of our calculations.

2 EVOLUTION OF RADIO GALAXY LOBES FOR FRII SOURCES

2.1 The KDA97 model

The KDA97 model of the dynamical expansion of an FR II-type radio source assumes a self-similar expansion, driven by twin jets emerging from the nucleus in opposite directions, pushing the surrounding environment. The jets produce strong shocks where the jet particles are accelerated and these particles made the cocoon expand. The density distribution in the ambient medium is assumed to be a power-law, $\rho(r) = \rho_0(r/a_0)^{-\beta}$, where ρ_0 is the density at a core radius a_0 . If the jet power is denoted by Q_j , then the combination $(Q_j/\rho_0 a_0^\beta)^{\frac{1}{5-\beta}} t^{\frac{3}{5-\beta}}$ has the dimension of length, and, in a self-similar model, it is proportional to the length of the jet, $L_j(t)$ (Falle 1991). Half of the cocoon volume is approximated by a cylinder of length L_j and a base radius. The ratio R between the length and half-width of this cylinder is referred to as its axial ratio.

The dynamics of the cocoon is determined by the cocoon pressure, $p_c = (\Gamma_c - 1)(u_e + u_B)$, where the contributions from different components have been added: (a) relativistic electrons with energy density u_e and adiabatic index Γ_c and (b) a tangled magnetic field with energy density u_B . (This implicitly assumes that $\Gamma_c = 4/3$, the adiabatic index appropriate for magnetic field pressure.) Suppose the cocoon volume scales as t^{a_1} . Then the cocoon pressure evolves with time as $p_c \propto t^{-\Gamma_c a_1}$ (see KDA97). The cocoon is assumed to be divided into small volume segments filled with magnetized plasma and particles that are injected into the cocoon at the jet terminal shock.

The initial electron energy distribution is assumed to be a power law in energy,

$$n(\gamma_i, t_i) d\gamma = n_0 \gamma_i^{-p} d\gamma_i \quad (1)$$

where the spectrum ranges between γ_{min} and γ_{max} . The electrons lose energy through adiabatic expansion, synchrotron and inverse Compton losses. KDA97 found a closed-form solution for the energy distribution at a later time $n(\gamma, t)$ in the case of a self-similar expansion of the cocoon.

The ratio of the energy density in particles to that in magnetic field is assumed to be r , so that the magnetic energy density u_B at time t is given by,

$$u_B(t) = \frac{r p_c(t)}{(\Gamma_c - 1)(r + 1)}. \quad (2)$$

Assuming that for synchrotron radiation, electrons emit only at their critical frequency $\nu = \gamma^2 \nu_L$, where ν_L is the Larmor frequency, the total radio power emitted by electrons in a volume element δV of the cocoon (radio power per unit frequency and solid angle) is given by,

$$\delta P_\nu = \frac{1}{6\pi} \sigma_T c u_B \frac{\gamma^3}{\nu} n(\gamma) \delta V. \quad (3)$$

Here the volume element at time t is related to the initial time interval over which the particles residing in it were injected, as,

$$\delta V(t) = \frac{(\Gamma_c - 1) Q_j}{p_c(t_i)} (4R^2)^{(1-\Gamma_c)/\Gamma_c} \left(\frac{t}{t_i}\right)^{a_1} \delta t_i. \quad (4)$$

The total radio power is then calculated by integrating over all time,

$$P_\nu = \int_0^t \delta P_\nu, \quad (5)$$

using eqns (3) and (4).

2.2 Evolution without self-similarity

In this paper, we would like to study the evolution of radio and X-ray power on a time scale that is longer than the typical jet lifetime, and study the effect of the stopping of jets on the X-ray emission. As we will explain later in the paper, the stopping of the jet has important effects on X-ray power of the cocoon, and the results are markedly different than in the case where the jet continues to be active. To do this, we cannot use the self-similar evolution assumed in KDA97. Instead, we calculate the size evolution the radio lobe in the following way that captures the basic physical processes in a simple manner.

Following the standard evolutionary picture (Scheuer 1974; Begelman & Cioffi 1989, Reynolds & Begelman 1997), that radio jets inject relativistic particles into a cocoon, which is overpressured (Nath 1995) and drive a strong shock into the ambient medium. The speed with which this shocked shell expands is determined by the ram pressure of the ambient gas that enters the shock. Assuming that the pressure inside the cocoon at any given time is uniform (see KA97), and a value $p_c(t)$, and assuming that radiation loss is small, we have for the expansion of the cocoon,

$$\begin{aligned} Q_j(t) &= \frac{1}{\Gamma_c - 1} (V_c \dot{p}_c + \Gamma_c p_c \dot{V}_c) \\ \frac{dL_j}{dt} &= \sqrt{\frac{p_c}{\rho_0}}, \end{aligned} \quad (6)$$

where V_c is the volume of the cocoon, and ρ_0 is the ambient density. For simplicity, we assume a constant axial ratio R , and the volume is assumed to be, $V_c = \frac{\pi}{4R^2} L_j^3$ (KA97).

For the jet luminosity we specify a jet lifetime t_j , so that Q_j is a constant for $t \leq t_j$, and $Q_j = 0$ for $t > t_j$, where $t_j \sim 10^{7-8}$ yr. Numerical simulations of 'dead' radio galaxies after the cessation of jet activity have shown that

the overpressured cocoon continues to expand until a pressure equilibrium is established with the ambient medium (Reynolds, Heinz, Begelman 2002).

We assume a constant axial ratio $R \sim 2$, which is an average value (Leahy and Williams 1984), and, following Wang & Kaiser (2008), we use a profile of the ambient density as given by,

$$\rho_a = \rho_0(r/a_0)^{-\beta} = \Lambda r^{-\beta}, \quad (7)$$

where $\Lambda = \rho_0 a_0^\beta$. For $\beta = 2$, Λ has the units of $[\text{g cm}^{-1}]$, and one can infer its value from the observations of environments of radio galaxies. Typically, for $\beta = 2$ and $a_0 \sim 200$ kpc, an electron density $n_{e,0} (\equiv \rho_0/(\mu m_p)) \sim 10^{-4} \text{ cm}^{-3}$ would imply $\Lambda \sim 10^{19} \text{ g cm}^{-1}$, a value we assume for most of our models in this paper. Observations of individual galaxies show Λ to be in the range of $10^{19-20} \text{ g cm}^{-1}$ (Fukazawa et al. 2004), whereas Jetha et al. (2007) inferred $\Lambda \sim 10^{19-10^{20}} \text{ g cm}^{-1}$ in group environments, although these determinations assume $\beta \sim 1.5$. For simplicity, because of the ability of combining two free parameters (ρ_0 and a_0) into one (Λ), we assume a value of $\beta = 2$ for our calculations.

Solving equations 6, we can therefore determine the cocoon pressure $p_c(t)$ at any instant, from which we determine an equipartition value of magnetic field, using eqn (2). assuming (as in KDA97) a ratio r between particle and magnetic field energy density. The corresponding electron energy density is then given by $u_e(t) = u_B(t)/r$, assuming that there is no thermal particles in the cocoon (i.e., in the language of KDA97, $u_T = 0$).

In the KDA97 model, particles are assumed to be injected at the termination point of the jet. In our case, after the jet stops, the injection of particles also stops, and so the integration in the equation (5), for the determination of radio power at a given time t , has an upper limit of $\min(t, t_j)$. To perform this integration, we rewrite the equation for volume segments (eqn (4)) which in the KDA97 model used the exponent a_1 for self-similar evolution of cocoons. For $t \leq t_j$, any small volume segment of the cocoon at a given instant t can be related to the pressure at the time (t_i) when the electrons in this segment were injected into the cocoon. One can rewrite equation (4) in the KDA97 model as (for $t < t_j$)

$$\delta V(t) = \frac{(\Gamma_c - 1)Q_j}{p_c(t_i)} (4R^2)^{(1-\Gamma_c)/\Gamma_c} \left(\frac{p_c(t)}{p_c(t_i)} \right)^{1/\Gamma_c} \delta t_i. \quad (8)$$

The evolution of Lorentz factor is explicitly solved using the loss equation,

$$\frac{d\gamma}{dt} = -\frac{1}{3} \frac{1}{V_c} \frac{dV_c}{dt} - \frac{4}{3} \frac{\sigma_T}{m_e c} \gamma^2 (u_B + u_c), \quad (9)$$

where the first term denotes adiabatic energy loss and is computed using the results of equations (6)). The second term combines radiation loss in synchrotron and inverse-Compton scattering. Here $u_c = aT_{CMB}^4$ is the CMB photon energy density, σ_T is the Thomson cross-section, m_e is the electron mass and c is the speed of light.

Thus, beginning with an initial energy distribution law with a power-law index p , one can solve for the energy distribution at any given time, $n(\gamma, t)$, given the initial distribution, $n(\gamma_i, t_i)$. Note that this was analytically done by KDA97 for a self-similar evolution of the cocoon, and we explicitly solve it in order to go beyond self-similarity.

Using this knowledge of $n(\gamma, t)$, we can then use equa-

tion (3) in conjunction with eqn (8), and integrate over time to calculate the radio power at a given frequency and at a given instant.

2.3 Inverse-Compton radiation

We extend this formalism further to determine the inverse-Compton (IC) emission as a function of time. Firstly, we note that electrons with Lorentz factor γ boosts a CMB photon of frequency ν_{CMB} into an energy $h\gamma^2\nu_{CMB}$. The precise calculation of the IC power for this photon would require one to consider the total spectrum of CMB photons. But we can simplify it for our purpose here by assuming all CMB photons to have a single frequency. We assume that the CMB photon distribution function is given by $v'(\epsilon) = v'_0\delta(\epsilon - k_B T_{CMB})$, where the normalizing factor v'_0 can be calculated by requiring that total energy density $\int \epsilon v'(\epsilon) d\epsilon = aT_{CMB}^4$, and one has $v'_0 = aT_{CMB}^4/k_B$. The total scattered power depends on the integral (see equation (7.29a) in Rybicki & Lightman 1979),

$$I' = \int d\epsilon v'(\epsilon) \epsilon^{\frac{p-1}{2}} = \frac{aT_{CMB}^3}{k_B} (k_B T_{CMB})^{(p-1)/2}. \quad (10)$$

If one had used the blackbody distribution function $v(\epsilon) = (8\pi\epsilon^2/h^3c^3)(\exp(\epsilon/k_B T_{CMB}) - 1)^{-1}$, then the corresponding integral would have yielded (see equation 7.31 in Rybicki and Lightman 1979),

$$I = \int d\epsilon v(\epsilon) \epsilon^{\frac{p-1}{2}} = \frac{8\pi}{h^3c^3} (k_B T_{CMB})^{\frac{p+5}{2}} \Gamma\left(\frac{p+5}{2}\right) \zeta\left(\frac{p+5}{2}\right), \quad (11)$$

where the symbols have the standard meanings. Then the ratio,

$$\frac{I'}{I} = \frac{\pi^4}{15} \frac{1}{\Gamma\left(\frac{p+5}{2}\right) \zeta\left(\frac{p+5}{2}\right)}, \quad (12)$$

shows the error one incurs in assuming all CMB photons to have the peak frequency in estimating the inverse Compton power. For $p = 2.2$, one finds $I'/I \sim 1.6$. Therefore the total scattered power calculated using this assumption is correct within an accuracy of 60%, and we adopt it for simplicity in our calculation.

We therefore calculate the IC power at a given frequency, in the manner of previous eqn (3), as,

$$P_{IC,\nu} = \int_0^{\min[t,t_j]} \frac{1}{6\pi} \sigma_T c u_c \frac{\gamma^3}{\nu} n(\gamma) \delta V, \quad (13)$$

using eqn (8) for δV , and the value of $n(\gamma, t)$ found from solving eqn (9).

Not all volume elements in the cocoon would contribute to the IC radiated power though. Electrons in some volume element that was injected at an earlier time t_i may lose energy to the extent that they fail to boost CMB photons to the observed X-ray band. These volume elements would not contribute to the X-ray power.

We calculate the total projected area of the cocoons that contribute to X-ray power, assuming the cocoon to be in the plane of the sky, and an axial ratio R . This allows us to calculate the X-ray surface brightness. We also calculate the fraction f_x of the total surface area of the cocoon that contributes to X-ray emission.

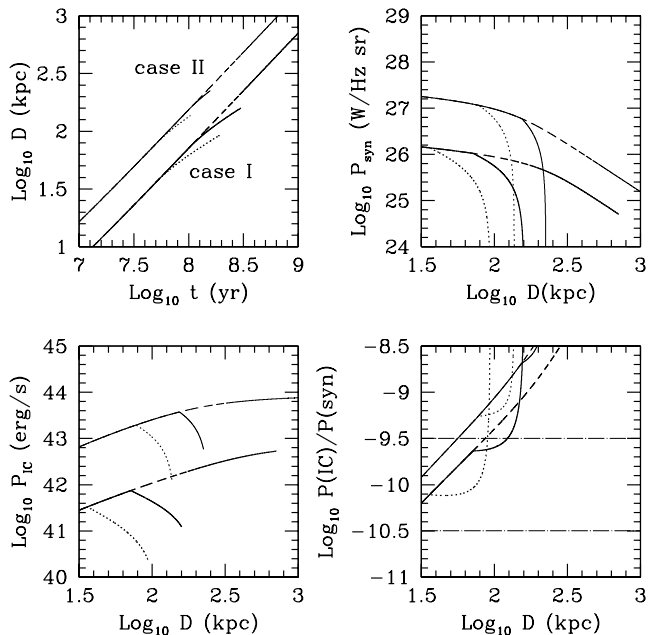


Figure 1. Time evolution of radio and X-ray powers are shown in this plot. Thick lines show the result for Case I ($Q_j = 10^{45}$ erg s $^{-1}$, $\Lambda = 10^{19}$ g cm $^{-1}$ at $z = 0.1$, with $\gamma_{min} = 1$), whereas thin lines show the results for Case II ($Q_j = 10^{46}$ erg s $^{-1}$ at $z = 1$, with the same ambient density as in Case I). Dotted, solid and dashed lines show the cases for $t_j = 5 \times 10^7$, 10^8 and 10^9 yr, respectively. Time evolution of the cocoon size (L_j) is shown in the top-left panel, radio power at 178 MHz (in W/Hz sr) in the top-right, and the inverse Compton power at 1 keV in the same units is shown in the bottom-left panel. The bottom-right panel shows the corresponding ratio of inverse Compton to radio power as a function of cocoon size for the three cases. Two horizontal dot-dashed lines indicate the range of observed ratios (see text).

3 RESULTS

To begin with, as a fiducial case, we consider $Q_j = 10^{45}$ erg s $^{-1}$, $\Lambda = 10^{19}$ g cm $^{-1}$ at $z = 0.1$, and a constant axial ratio $R = 2$. Following KDA97, we also adopt $r = 0.785$ and $p = 2.14$, $\gamma_{max} = 10^6$ and $\gamma_{min} = 1$. We refer to this set of parameters as Case I.

The set of thick lines in Figure 1 show the results for this fiducial case. We plot the time evolution of cocoon size in the top-left panel, radio power at 178 MHz in the top-right panel, IC power at 1 keV in the bottom-left panel. The corresponding evolution of the ratio of synchrotron to IC power with cocoon size is shown in the bottom-right panel. The solid lines show the case for $t_j = 10^8$ yr, and dotted and dashed lines show the cases $t_j = 5 \times 10^7$ and 10^9 yr, respectively.

In the same figure, we also show the results of another case, with a higher jet power and one located at a higher redshift than in the fiducial case. The thin set of lines in Figure 1 show the case with $Q_j = 10^{46}$ erg s $^{-1}$ at $z = 1$ (Case II), keeping the values of other parameters the same.

The evolution of the size of the cocoon is self-similar, as expected, till $t \sim t_j$ (top left panel of Figure 1), after which the cocoon size expands slower than before. The radio luminosity as a function of time (top-right panel) is comparable to the results of KDA97 for the case of $t_j \sim 10^9$ yr,

with sources at higher redshift dimming faster than their low redshift counterparts because of inverse Compton loss. For shorter jet lifetime, the radio luminosity drops precipitously after $t \sim t_j$. This is mainly driven by rapidly declining pressure inside the cocoon owing to adiabatic expansion.

The X-ray luminosity of the cocoon at 1 keV (bottom-left panel of Figure 1) increases till $t \sim t_j$, as high energy electrons lose energy ($dE/dt \propto E^2$) and enter the energy bins that are conducive for inverse Compton scattering CMB photons to the soft X-ray band. The number of electrons with Lorentz factors $\sim 10^3$ increase because the draining of these electrons to lower energy bins is more than compensated by the supply of energetic electrons from the jet. But after the jet stops, no new electrons are supplied to the cocoon, and the X-ray power drops rapidly (more so at high redshifts).

The time scale for inverse Compton loss is $t_{ic} \sim 3 \times 10^7$ yr for $\gamma \sim 10^3$ at present epoch. The time scale for the drop in X-ray power is made shorter than this by the additional loss of energy from adiabatic expansion of the cocoon. It is clear from curves in Figure 1 that the stopping of the jet activity has a profound effect on the X-ray power that would have been missed in a calculation with self-similar evolution of cocoons. Self-similar models would have predicted a rising X-ray power, although the rate of increase would have tapered beyond a time-scale $\sim t_{ic}$, because the loss of electron energy would have been continually compensated by injection of new and energetic electrons. In the case of jet stopping after t_j , this privilege is withdrawn from the cocoons and their X-ray power rapidly diminishes with time.

The ratio of X-ray to radio power (bottom-right panel), therefore, shows a mild increase till t_j , after which it increases rapidly, because of the drop in radio luminosities. We note that, typically the value of the ratio at $t \sim t_j$ is of order $P_{ic}/P_s \sim 10^{-10}$ – 10^{-9} . For a single power law electron energy distribution with index $p = 2\alpha + 1$, where α is the synchrotron (and inverse Compton) radiation spectral index, the ratio of relative luminosities can be written in terms of the strength of the magnetic field and the CMB temperature. For $p = 2.5$, we have (e.g. Tucker 1977),

$$\frac{P_{ic}}{P_s} \approx 4.7 \times 10^{-11} \left(\frac{T_{CMB}}{2.73 K} \right)^{3+\alpha} \left(\frac{B}{10 \mu G} \right)^{-(\alpha+1)} \quad (14)$$

where the coefficient is $\sim 2.7 \times 10^{-11}$ for $p = 2$, and 8.3×10^{-12} for $p = 3$. These values are somewhat lower than predicted from our detailed calculations, which take into account the electron energy distribution in different parts of the cocoon as they evolve. Although the magnetic field strength throughout the cocoon is assumed to be the same at any given time, the difference in the evolution of electron energy spectrum in different parts of the cocoon can give rise to a value of the ratio P_x/P_r that is different from the above simple estimate. Admittedly, the flux ratio is mainly driven by magnetic field, which is what the above simple estimate indicates, but our calculations show the important role played by the evolution of electron spectrum prior to the observed epoch for an object.

The observed ratios of fluxes at 1 keV and 178 MHz fall in the range of $P_x/P_r \sim 10^{-10.5}$ – $10^{-9.5}$, for objects with a variety of linear sizes and at different redshifts (e.g., 3C 215 ($z = 0.41$), 3C 334 ($z = 0.56$), 3C 9 ($z = 2.0$) (Bridle et al. 1994), 3C 219 ($z = 0.17$) (Perley et al. 1980),

3C 265 ($z = 0.81$) (Bondi et al. 2004), 3C 109 ($z = 0.31$) (Giovannini et al. 1994), 3C 179 ($z = 0.85$) (Sambruna et al. 2002)). We indicate this range by two dot-dashed lines in the figure. Since the evolution of this ratio depends on many parameters (as listed in Table 1, for example), our goal in this paper is not to reproduce all the observed parameters, but to probe whether or not the model yields representative values consistent with observations.

It is apparent from the figure that the observed range of ratios are mostly consistent with model predictions for different parameters. It also appears that the observed range is *not* related to the rapidly rising part of the evolutionary curves. In other words, the systems observed in X-ray (near 1 keV) should also be radio bright at low frequencies, of order ~ 150 MHz, that we have used for our calculations (~ 178 MHz). Low frequency radio observations therefore should be an important probe of X-ray bright cocoons, as has been pointed out by previous authors.

Another aspect is that cocoons spend a relatively short time in the rapidly rising parts of the curves for ratio between P_x/P_r , because of the precipitous drop in radio luminosity after t_j . In other words, radio galaxies that have faded from the window of frequencies of order a few hundred MHz, are unlikely to be X-ray bright, since the X-ray power would also drop (see bottom-left panel of Figure 1).

Next, we plot in Figure 2 the corresponding flux in the 1-5 keV band (top left panel) for the cases shown in Figure 1. Our results show that for the parameters used here the cocoons typically emit at a flux of $\sim 10^{-14}$ erg s $^{-1}$ cm $^{-2}$ per keV (or a few micro-Crab) before dropping after t_j , consistent with observed fluxes (see, e.g., Laskar et al. 2010).

We also need to consider the X-ray surface brightness apart from the total flux. We calculate the total area of the X-ray bright region of the cocoon, by summing over the volume elements in which electrons contribute to the X-ray emission in the 1-5 keV band, and projecting in the plane of the sky. This is shown in the bottom-left panel of Figure 2, which suggests that for cocoons larger than 100 kpc, typically a patch as large as tens of arcseconds would be X-ray bright. If one estimates the fraction of the cocoon area that is X-ray bright, this fraction initially rises (till t_j) to $\sim 0.3 - 0.5$ of the total area (assuming the cocoon the projected in the plane of the sky), and then drops.

This calculation of the angular size of the X-ray bright region of the cocoon allows us to estimate an average X-ray surface brightness of the cocoon, and we show the results in the top-right panel of Figure 2, for the same cases as mentioned earlier. The surface brightness (in the 1-5 keV band) initially drops in a gradual manner, owing to two competing effects: increasing X-ray luminosity and an increasing portion of the cocoons which are illuminated by X-ray. But it drops rapidly after t_j , especially at high redshift.

Another important probe of X-ray bright cocoons is the X-ray spectral index. We calculate the photon index $\Gamma (= \alpha + 1)$ in the 1-5 keV band for the same cases, and the results are shown in the bottom-right panel of Figure 2. We also include data points for a number of cases which have been observed long enough for spectrum determination. We have estimated the cocoon angular size from visual inspection from the observations cited in the caption, assuming the cocoons to be projected in the plane of the sky, and estimated the physical size assuming a Λ -CDM cosmology

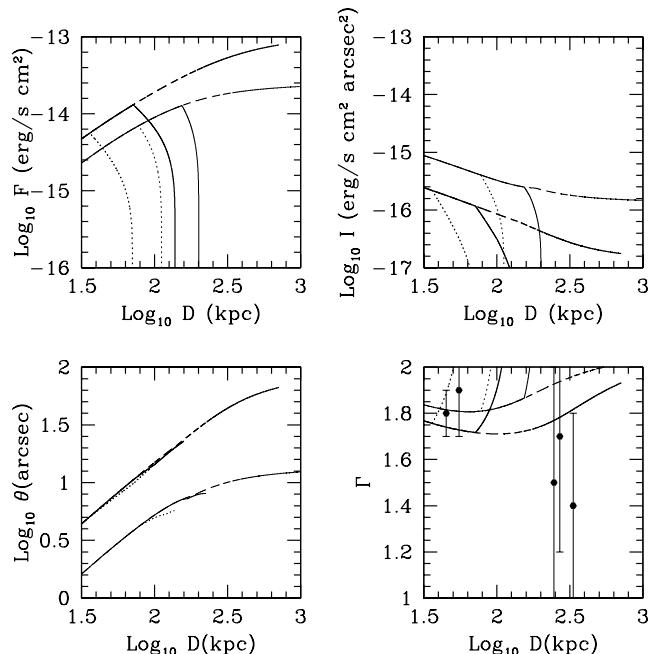


Figure 2. Evolutions of X-ray flux in the 1-5 keV band (top-left panel), X-ray surface brightness (top-right), angular size of the X-ray bright region (bottom-left) are shown as functions of the cocoon length, for the same cases as in Figure 1. Thick lines refer to the fiducial case of $Q_j = 10^{45}$ erg s $^{-1}$, $\Lambda = 10^{19}$ g cm $^{-1}$ at $z = 0.1$, with $\gamma_{min} = 1$ (Case I). Thin lines consider $Q_j = 10^{46}$ erg s $^{-1}$ at $z = 1$ (Case II). Solid, dotted and dashed lines show the cases for $t_j = 5 \times 10^7$, $\times 10^8$ and 10^9 yr, respectively. The bottom right panel shows the corresponding X-ray photon index in the 1-5 keV band as a function of cocoon size for these cases. We also plot the data points for 3C 47N ($z = 0.43$, $L_j \sim 333$ kpc), 3C 215 ($z = 0.41$, $L_j \sim 246$ kpc) (Bridle et al. 1994), 3C 219 ($z = 0.17$, $L_j \sim 270$ kpc), 3C 452 ($z = 0.81$, $L_j \sim 45$ kpc) (Perley et al. 1980), 3C 265E ($z = 0.81$, $L_j \sim 55$ kpc) (Bondi et al. 2004), for comparison.

with $h = 0.7$, $\Omega_0 = 0.3$, $\Omega_\Lambda = 0.7$. The error bars on the data points are large, but there appears to be a trend of decreasing photon index with increasing cocoon size: larger cocoons show flatter X-ray spectrum.

Our model predictions show that initially the X-ray spectrum gradually gets flatter (smaller value of Γ) till $t \sim t_j$. This is because of the fact that for electrons $\gamma \geq 10^3$, the injection of fresh particles mitigates the radiative steepening of electron spectrum. The injection of electrons from the jet compensates for synchrotron energy losses for electrons with $\gamma \sim 10^3$, where two relevant time scales become comparable: (a) the jet lifetime (10^{7-8} yr) and the (b) inverse Compton cooling time scale of electrons with $\gamma \sim 10^3$ ($\sim 3 \times 10^7$ yr at present cosmological epoch). This energy scale (corresponding to $\gamma \sim \sqrt{1 \text{ keV } kT_{CMB}} \sim 2 \times 10^3$) also happens to be the one required to upscatter CMB photons to keV range. The concurrence of these two timescales produces a temporary hardening of the soft X-ray spectrum.

Then, after the jet stops, the number of electrons at this energy scale rapidly decreases because of inverse Compton and adiabatic loss, and the spectrum becomes soft again. This softening occurs rapidly at high redshift, as expected from increasing inverse Compton loss. With regard to some of the data points with large cocoons and $\Gamma \sim 1.5$, we found

Model	Q_j (erg s $^{-1}$)	z	t_j (yr)	Λ (g cm $^{-1}$)	γ_{min}
Case I	10^{45}	0.1	10^8	10^{19}	1
Case II	10^{46}	0.1	10^8	10^{19}	1
Case III	10^{46}	0.2	10^8	10^{19}	1

Table 1. The values of different parameters used in the models cited in the text are tabulated here. Apart from these parameters, all models use $\beta = 2$, $\Gamma_c = 4/3$, $R = 2$.

that they can be explained with models using a jet power of order 10^{46} erg s $^{-1}$ at low redshifts.

3.1 Variations with parameters

Although we have shown the results for cocoons for a few cases, varying parameters such as the jet power, redshift and jet life time, there are other free parameters in this model whose effects must be understood. The X-ray properties of cocoon also depend on the ambient density (here parametrized as Λ) and the lower cutoff in the electron energy distribution (γ_{min}). To study the effect of these parameters, we first plot in Figure 3 (with solid lines) the results for a fiducial case (Case III): $Q_j = 10^{46}$ erg s $^{-1}$, $z = 0.2$, $t_j = 10^8$ yr, and $\Lambda = 10^{19}$ g cm $^{-1}$, $\gamma_{min} = 1$. In this section we will study the effect of changing the values of L_j , Λ , γ_{min} separately, and compare with the results for our fiducial case. We will not vary the redshift and the jet life time, as the discussion in the previous section has already considered the effects of changing these parameters. Also, we keep γ_{max} fixed at 10^6 , and we do not change the values of p and r .

In Figure 3, we have plotted the X-ray flux (in 1-5 keV band; top-left panel), ratio between X-ray and radio power (top-right panel), X-ray surface brightness (in 1-5 keV; bottom-left panel), and the photon index (Γ) in the bottom-right panel. All these parameters are plotted against the cocoon size.

First, the results for the fiducial case mentioned above are shown with solid lines in all panels for easy comparison. Then, with dotted line, we show the results of changing jet power to 10^{47} erg s $^{-1}$. As expected this cocoon expands to occupy a large volume, and is more X-ray bright than the fiducial case. The ratio of X-ray to radio power does not change, however, but the surface brightness increases. The photon index continues to decrease and the X-ray spectrum becomes harder with time (and size) for $t \sim t_j$ after which it becomes softer.

Next, we change the value of γ_{min} to 10^3 (keeping all other values same as in the fiducial case), and the results are shown with short-dashed lines. Increasing the lower cutoff results in increasing the number density of electrons for a given total energy in the cocoon, and produces a larger X-ray flux and surface brightness. But since there are more electrons with high energy in this case compared to the fiducial case, they also lose energy faster, and consequently, the drop in X-ray power after the stopping of the jet is faster than in the fiducial case. Interestingly, the increasing of γ_{min}

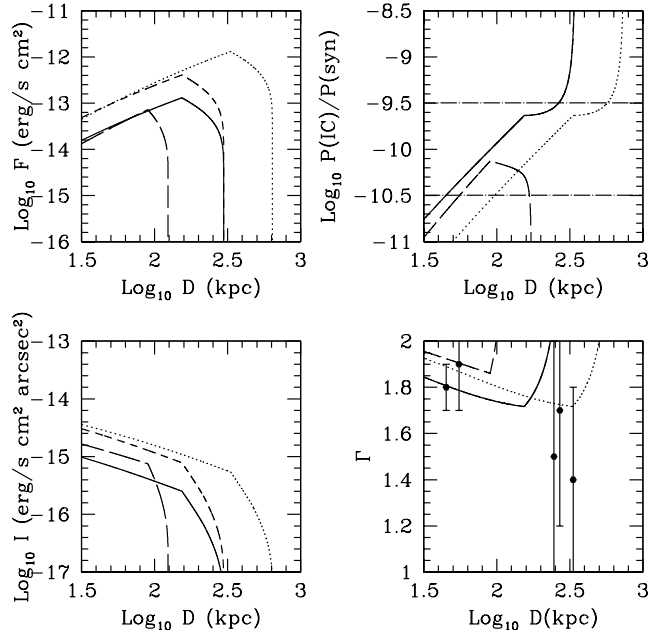


Figure 3. Evolutions of the X-ray flux (in 1-5 keV band; top-left panel), ratio of X-ray to radio power (top-right), X-ray surface brightness (bottom-left) and X-ray photon index (bottom-right) are shown as functions of the cocoon size for a few cases. The solid line shows the results for Case III: $Q_j = 10^{46}$ erg s $^{-1}$, $\Lambda = 10^{19}$ g cm $^{-1}$ at $z = 0.2$, with $\gamma_{min} = 1$, and $t_j = 10^8$ yr. The dotted line shows the case for $Q_j = 10^{47}$ erg s $^{-1}$, keeping other parameters fixed. The short-dashed lines refer to the case with $\gamma_{min} = 10^3$, and the long-dashed lines show the effect of changing the ambient density to $\Lambda = 5 \times 10^{19}$ g cm $^{-1}$. Data points from Figure 2 for photon index are again plotted here.

does not effect the the X-ray to radio power ratio and the X-ray photon index. (It would, if the lower cutoff were to increase beyond $\gamma \sim 10^3$.)

Finally, we change the ambient density to $\Lambda = 5 \times 10^{19}$ g cm $^{-1}$ that is indicative of a dense environment. The results are shown with long-dashed lines, and they show that the radio cocoon is constrained to remain small in size in this case. This results in not allowing the cocoon pressure (and magnetic field) to decrease fast enough, so that electrons are made to lose energy faster through synchrotron radiation. Both X-ray and radio power drop rapidly in this case and the ratio between X-ray to radio power also decreases (although, since the curves are drawn as functions of D , the rapid decrease is not apparent from the figures). The photon index also hardens faster than in the fiducial case. This implies that it would be difficult to detect X-ray bright cocoons in dense environments like galaxy clusters, although it would be difficult to observe them anyway because of the bright X-ray emission from the intracluster gas.

The X-ray fluxes shown in the top-left panel of Figure 3 suggest that for typical radio galaxy parameters as used here, the cocoons shine in soft X-rays with a flux of 1–10 micro-Crab, or, 10^{-14} – 10^{-13} erg cm $^{-2}$ s $^{-1}$ per keV, before dropping to lower values after t_j .

Curves in the top-right panel of Figure 3 show that the ratio of X-ray to radio power is a robust parameter, in the sense that it does not vary with changes in γ_{min} and jet

power at fixed times. The curves are plotted against D , but the kink in the curves due to the stopping of jet occurs for all curves at the same time, namely, t_j , and a comparison of the solid, short dashed (which happens to be superposed on the solid curve) and the dotted curves show that the ratio is a robust parameter. It does vary with redshift (as we have seen in Figure 1) and with ambient density (long dashed line in Figure 3). This robustness allows us to use this parameter to characterize the connection between radio and X-ray properties of cocoons, and we will discuss this issue further in the next section.

3.2 Time-averaged ratio of X-ray to radio power

Our results show that many of the X-ray properties of FR-II radio galaxy cocoons vary substantially with time, even when all other parameters such as jet power, ambient density and others are kept constant. It is therefore not easy to predict the X-ray properties of these sources that can be tested with observations, because it is difficult to determine the age of these sources from radio or other observations.

One can however use the fact that the evolutionary time-scale of radio galaxies, of order a few hundred Myr, is much shorter than the Hubble time, even at redshifts when the radio galaxy population peaked in number density ($z \sim 2$). This implies that one can use time-averaged quantities related to X-ray emission, and speculate upon their average properties that could be observed and tested.

In particular, we would like to determine the average property of the ratio of luminosities in X-ray and radio frequencies, $\nu_x P_x / \nu_r P_r$ of the sources under consideration, averaged over time until their X-ray or radio emission drops rapidly: $\int \frac{\nu_x P_x}{\nu_r P_r} dt / \int dt$. Our results (Figure 3, top-right panel) shows that this ratio of luminosities is a robust parameter, and it varies negligibly with the variations in jet power, lower cut-off in γ , although it varies strongly with changes in ambient density. This ratio is however likely to increase with redshift, and we wish to determine the scaling with redshift.

We therefore compute the X-ray luminosity $\nu_x P_x$ in the 1-5 keV band, and we choose a radio frequency of $\nu_r = 151$ MHz to compute $\nu_r P_r$. We compute a time-average of this ratio, summing over the duration in which the sources are both X-ray and radio bright in these frequencies (in the source frame).

Celotti & Fabian (2004) have discussed the significance of this ratio of X-ray and radio luminosities in the case of radiation from electrons with a single power law energy distribution. In this case, this ratio can be written as,

$$\frac{\nu_x P_x}{\nu_r P_r} = \frac{U_{CMB}}{U_B} \left(\frac{\nu_x \nu_B}{\nu_r \nu_{CMB}} \right)^{1-\alpha} (1+z)^{3+\alpha}, \quad (15)$$

where α is the radio spectral index, U_{CMB} and U_B are the energy density in CMB photons (at $z = 0$) and magnetic field, respectively. Also, ν_B and ν_{CMB} are the gyrofrequency and the peak frequency of CMB photons at present epoch. For a field strength of $B = 0.1\text{--}10 \mu\text{G}$, the ratio between the luminosities at 1 keV and 151 MHz (in the observer frame) can take values 0.08–300 at $z = 0$, for $p = 2.6$, and 0.08–50 for $p = 2$. The ratio increases with redshift, although the increase can be mitigated by the possibility that magnetic field may change with redshift. Celotti & Fabian chose a

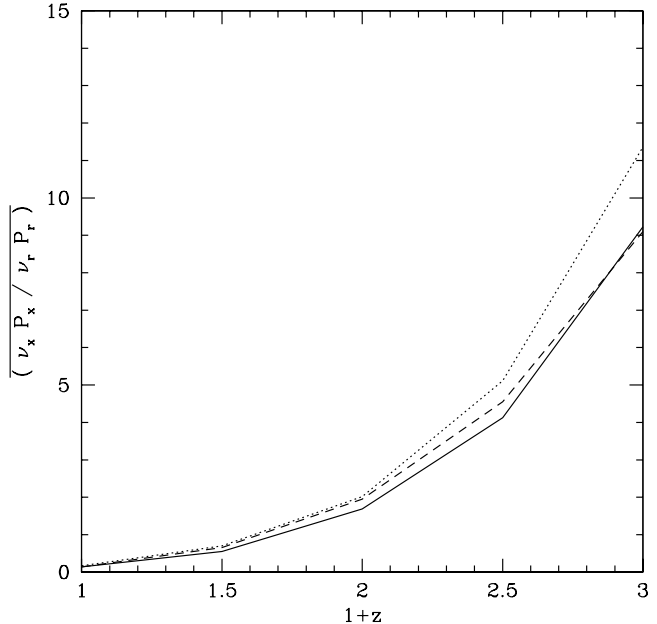


Figure 4. Time-averaged ratio between X-ray and radio luminosities is shown as a function of source redshift, for $p = 2.5$ (solid line), and $p = 2.14$ (dotted line). The fit ($\sim 0.14(1+z)^{3.8}$) is shown with a dashed line.

conservative value of unity for this ratio, at all redshifts, and discussed the possible implications.

In our model that includes evolving electron populations, there is no single power law energy distribution of electrons, and the magnetic field is estimated through equipartition arguments. We show the evolution of the time-averaged ratio of X-ray and radio luminosities at the above mentioned frequencies (in the source frame) with redshift in Figure 4, for two values of $p = 2.5$ (solid line), and $p = 2.14$ (dotted line), the last choice of p being motivated by KDA97. Interestingly, the difference between these two initial values of p is not large, and makes the time-averaged ratio of luminosities a robust quantity. We find that the case for $p = 2.5$ can be fitted with a simple scaling with redshift,

$$\overline{(\nu_x P_x / \nu_r P_r)_t} \sim 0.14(1+z)^{3.8}. \quad (16)$$

The results of the two cases of different values of p are different from the expectation from the simple formula mentioned above. The X-ray to radio luminosity increases with decreasing p (or increasing α), especially at high redshift. This is because the increased population of high energy electrons (for smaller values of p) rapidly lose energy, decreasing γ down to the level where they become X-ray bright, and this process become more efficient at high redshift.

3.3 X-ray luminosity function of FR-II radio galaxies

We are now in a position to estimate the number density of X-ray bright radio galaxy cocoons using the radio luminosity function of these sources, and using the above results for the relation between X-ray and radio emission. We use the radio luminosity function of FR-II galaxies, as determined

by Willott et al. (2001) from 3CRR, 6CE and 7CRS samples. This luminosity function was determined assuming a cosmological model with $\Omega_0 = 0 = \Omega_\Lambda$, $\Omega_k = 1$, $h = 0.5$. We have converted it for the Λ -CDM cosmology with $\Omega_\Lambda = 0.7$, $\Omega_m = 0.3$, $h = 0.7$ using the relation (Peacock 1985),

$$\rho_1(P_1, z) \frac{dV_1}{dz} = \rho_2(P_2, z) \frac{dV_2}{dz} \quad (17)$$

where P is the luminosity derived in a specific cosmological model for a measured flux and at a given redshift z , and the indices refer to the two different cosmological models. The luminosities in two different models are related as,

$$P_1 D_1^{-2} = P_2 D_2^{-2}, \quad (18)$$

where

$$D(z) = \frac{c}{H_0} \int_0^z \frac{dz'}{\sqrt{\Omega_M(1+z')^3 + \Omega_\Lambda}}, \quad (19)$$

is the comoving distance in a flat cosmological model. Also, the comoving volume in eqn 17 is given by $dV = 4\pi D(z)^2 dD(z)$.

Having done this, we have associated a diffuse X-ray luminosity to each FR-II sources with the scaling result from the last section, and determined the X-ray luminosity function of FR-II galaxies.

Figure 5 shows the computed X-ray luminosity function, in the units of number per unit (comoving) Mpc^3 , per 10^{44} erg s^{-1} , for three redshifts: $z = 0$ (solid), $z = 1$ (dotted) and $z = 2$ (short-dashed line). The peak of the X-ray luminosity function shifts to increasing luminosity because of the strong redshift evolution of the X-ray to radio power ratio. We note that Celotti & Fabian (2004) assumed a constant ratio of unity and so their X-ray luminosity function peaked at the same luminosity at different redshifts (their Figure 3).

We compare the computed luminosity function with that of clusters in X-ray in the 0.5-2 keV band (shown here with long-dashed line) as determined from the REFLEX sample by Böhringer et al. (2002) (for a similar cosmology but with $h = 0.5$). Recently, Mullis et al. (2004) found that the cluster X-ray luminosity function decreases with increasing redshift at the high luminosity end, but does not evolve significantly below 10^{44} erg s^{-1} . The comparison with the luminosity function expected from FR-II galaxies shows that the number density of these sources become comparable at the high luminosities at $z \sim 2$.

We can also estimate the number of diffuse X-ray emitting cocoons in a given area of the sky above a given X-ray flux limit. Integrating the above luminosity function to $z \sim 2$, we find that the number of sources above a flux limit of $\sim 3 \times 10^{-16}$ $\text{erg cm}^{-2} \text{s}^{-1}$ is of order ~ 27 per square degree. Recently Finoguenov et al. (2010) detected ~ 6 X-ray emitting radio lobes in 1.3 deg^2 above 2×10^{-15} $\text{erg cm}^{-2} \text{s}^{-1}$, and given the uncertainties, our estimate is consistent with it. .

4 DISCUSSION

The expected number of X-ray bright radio galaxy cocoons as estimated above can be compared with the observed values. Bauer et al. (2002) found six extended sources in the *Chandra* Deep Field North survey, within an area of ~ 130

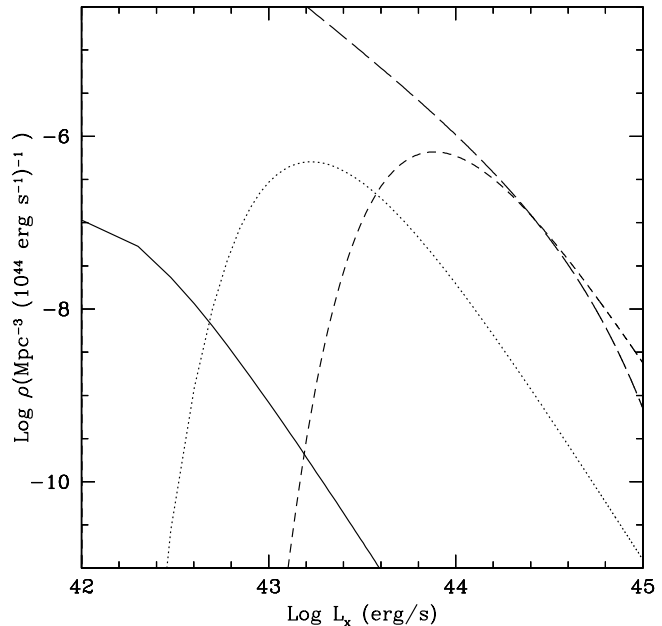


Figure 5. Predicted X-ray luminosity function of FR-II radio galaxy cocoons, based on the relation between X-ray and radio power, is shown here, for $z = 0$ (solid), $z = 1$ (dotted) and $z = 2$ (short-dashed line). The X-ray luminosity refers to that in the 1-5 keV band, and the luminosity function shows the comoving number density of objects, per 10^{44} erg s^{-1} , in the Λ -CDM cosmology, with $h = 0.7$. The long-dashed line shows the present day X-ray luminosity function of clusters, based on the REFLEX (Rosat-ESO Flux Limited) survey by Böhringer et al. (2002).

arcmin^2 , implying a surface density of $\sim 167_{-67}^{+97} \text{ deg}^{-2}$, at a limiting soft X-ray flux of $\sim 3 \times 10^{-16}$ $\text{erg cm}^{-2} \text{s}^{-1}$. Our estimate shows that a small fraction of order ~ 0.1 – 0.3 of such extended soft-X-ray sources in the sky could be due to FR-II radio galaxies.

The X-ray luminosity function in the soft band can also be used to estimate mirror effect of X-ray emission, namely, the Sunyaev-Zeldovich (SZ) effect on the CMB. To some extent, it would underestimate the effect because of the fact the soft-band X-ray power is smaller than the total X-ray power. Keeping this in mind, we can determine the ratio of the total radiation energy density in the soft-X-ray band that is emitted by these sources and that is present in the CMB, by integrating the luminosity function: $\frac{\Delta\epsilon}{\epsilon} \sim \int \frac{dt}{dz} \frac{dz}{aT_{CMB,z}^4} \int L_x \frac{d\rho(L_x, z)}{dL_x} dL_x$. We find that $\Delta\epsilon/\epsilon \sim 2 \times 10^{-7}$, integrating up to a redshift $z \sim 2$, although strictly speaking this is a lower limit. This implies a Compton y -parameter of order $y \sim (1/4) \frac{\Delta\epsilon}{\epsilon} \geq 10^{-7}$. Yamada, Sugiyama & Silk (1999) considered the distortion of the CMB from the population of radio galaxy cocoons, using Press-Schechter mass function and assuming that halos above a certain mass limit produce radio galaxies, and estimated that $y \sim 6 \times 10^{-5}$. Enblin & Kaiser (2000) however estimated from radio galaxy luminosity functions a total optical depth of the relativistic electrons to be $\tau \sim 10^{-7}$. For relativistic electrons with $\gamma_{min} \geq 1$, one has $y_{nth} \geq \tau$, and our estimate is consistent with that of Enblin & Kaiser (2000).

It is not only the cocoons of radio galaxies that have

been observed in X-rays, but the jets have also been recently detected by *Chandra* (e.g., Schwartz 2002). Although some uncertainties remain in identifying the emission mechanism behind the X-ray radiation, inverse Compton scattering of CMB photons is thought to be one of the possibilities (Stawarz et al. 2004). It is possible that the X-ray radiation from the jets may contaminate the emission from the cocoons and make the study of cocoons in X-rays difficult, especially at high redshift where angular resolution may become an issue.

5 CONCLUSION

We have used an evolving model of FR-II radio galaxy cocoons that takes into account the stopping of the jet after a jet lifetime of t_j , and we have studied the X-ray property of cocoons from inverse Compton scattering of CMB photons. We have shown that the X-ray power (in the 1-5 keV band) and the X-ray surface brightness decrease rapidly after the stopping of the jet, as well as the radio power. At the same time, the X-ray photon index is found first decrease to some extent while the jet is active. This occurs because at the important energy scale for inverse Compton scattering of CMB photons to keV range ($\gamma \sim 10^3$), two relevant timescales become comparable: the jet lifetime and that of cooling due to inverse Compton (10^{7-8} yr). After the stopping of the jet, the photon index increases, making the spectrum softer. We find that typical radio galaxy parameters produce an X-ray flux (1-5 keV band) of order 1–10 μ -Crab, being emitted from regions with sizes of order of tens of arcsec.

We have also shown that the ratio of X-ray to radio power changes little with jet power and lower cut-off in the electron energy distribution, and it changes mostly with redshift and ambient density. We have then determined the time-averaged ratio of X-ray to radio power and studied its scaling with redshift, which we found to scale as $\propto (1+z)^{3.8}$, almost independent of the injected electron energy spectrum, contrary to the expectations from a population of electrons with a single power law distribution of energy.

Using these scaling relations, we estimated the X-ray luminosity function of FR-II radio galaxies at various redshifts, and estimated the number of such diffuse X-ray sources to be ~ 25 deg $^{-2}$ above an X-ray flux limit of $\sim 3 \times 10^{-16}$ erg cm $^{-2}$ s $^{-1}$ (compared to ~ 167 deg $^{-2}$ diffuse soft X-ray sources observed in the *Chandra* Deep Field North for a similar flux limit).

I am grateful to Paddy Leahy, the referee, for valuable comments. I also thank Mitchell Begelman for his comments on the paper and Biswajit Paul for discussions.

REFERENCES

Bauer, F. E. et al. 2002, *AJ*, 123, 1163
 Begelman, M. C. & Cioffi, D. F. 1989, *ApJ*, 341, 685
 Blundell, K. M., Fabian, A. C., Crawford, C. S., Erlund, M. C., & Celotti, A. 2006, *ApJ*, 644, L13
 Bondi, M., Brunetti, G., Comastri, A., & Setti, G. 2004, *MNRAS*, 354, 43

Böhringer, H. et al. 2002, *ApJ*, 566, 93
 Bridle, A. H., Hough, D. H., Lonsdale, C. J., Burns, J. O. & Laing, R. A. 1994, *AJ*, 108, 766
 Celotti, A. & Fabian, A. C. 2004, *MNRAS*, 353, 523
 Croston, J. H., Hardcastle, M. J., Harris, D. E., Belsole, E., Birkinshaw, M., Worrall, D. M. 2005, *ApJ*, 626, 733
 Enßlin, T. & Kaiser, C. 2000, *A&A*, 360, 417
 Erlund, M. C., Fabian, A. C., Blundell, K. M. 2008, *MNRAS*, 386, 1774
 Falle, S. A. E. G. 1991, *MNRAS*, 217, 149
 Fabian, A. C., Chapman, S., Casey, C. M., Bauer, F. & Blundell, K. M. 2009, *MNRAS*, 395, L67
 Felten, J. E., Rees, M. J. 1967, *Nat*, 221, 924
 Finoguenov, A. et al. 2010, *MNRAS*, 403, 2063
 Fukazawa, Y., Makishima, K. & Ohashi, T. 2004, *PASJ*, 56, 965
 Giovannini, G., Feretti, L., Venturi, T., Lara, L., Marcaide, J., Rioja, M., Spangler, S. R. & Wehrle, A. E. 1994, *ApJ*, 435, 116
 Jetha, N. N., Ponman, T. J., Hardcastle, M. J. & Croston, J. H. 2007, *MNRAS*, 376, 193
 Johnson, O., Almaini, O., Best, P. N., Dunlop, J. 2007, *MNRAS*, 376, 151
 Kaiser, C. R., & Alexander, P., 1997, *MNRAS*, 286, 215 (KA97)
 Kaiser, C. R., Dennett-Thorpe, J., & Alexander, P. 1997, *MNRAS*, 292, 723 (KDA97)
 Kaiser, C. R. & Cotter, G. 2002, *MNRAS*, 336, 649
 Komissarov, S. S. & Gubanov, A. G. 1994, *A&A*, 285, 27
 Isobe, N., Makoto, S. T., Gandhi, P., Hayato, A., Nagai, H., Hada, K., Seta, H., Matsuta, K. 2009, *ApJ*, 706, 454
 Rybicki, G. B. & Lightman, A. P. 1979, *Radiative Processes in Astrophysics* (Wiley, New York).
 Laskar, T., Fabian, A. C., Blundell, K. M. & Erlund, M. C., 2010, 401, L1500
 Nath, B. B. 1995, *MNRAS*, 274, 208
 Mullis, C. R. et al. 2004, *ApJ*, 607, 175
 Peacock, J. A. 1985, *MNRAS*, 217, 601
 Perley, R. A., Bridle, A. H., Willis, A. G., & Fomalont, E. B. 1980, *AJ*, 85, 499
 Reynolds, C. S. & Begelman, M. C. 1997, *ApJ*, 487, L135
 Reynolds, C. S., Heinz, S. & Begelman, M. C. 2002, *MNRAS*, 332, 271
 Sambruna, R., Maraschi, L., Tavecchio, F., Urry, C. M., Cheung, C. C., Chartas, G., Scarpa, R., & Gambill, J. K. 2002, *ApJ*, 571, 206
 Schwartz, D. A. 2002, *ApJ*, 569, L23
 Scheuer, P. A. G. 1974, *MNRAS*, 166, 513
 Stawarz, L., Sikora, M., Ostrowski, M. & Begelman, C. M. 2004, *ApJ*, 608, 95
 Tucker, W. H. 1977, *Radiation Processes in Astrophysics*, MIT Press
 Wang, Y. & Kaiser, C. R. 2008, *MNRAS*, 388, 677
 Willott, C. J., Rawlings, S., Blundell, K. M., Lacy, M. & Eales, S. A. 2001, *MNRAS*, 322, 536
 Yamada, M., Sugiyama, N. & Silk, J. 1999, *ApJ*, 522, 66